Available online at www.sciencedirect.com
SCIENCE DIRECT
Theoretical and Applied Fracture Mechanics 46 (2006) 57–69
theoretical and applied fracture mechanics
www.elsevier.com/locate/tafmec

Microstructure and fracture characteristic of Mg–Al–Zn–Si_3N_4 composites

S.R. Wang [a,b,*], H.R. Geng [c], Y.Z. Wang [c], J.C. Zhang [a]

[a] School of Mechanical Engineering, Jinan University, Jinan 250022, China
[b] The Key Laboratory of Liquid Structure and Heredity of Materials of Shandong University, Jinan 250014, China
[c] School of Material Science, Jinan University, Jinan 250022, China

Available online 22 June 2006

Abstract

Magnesium matrix composites reinforced by three dimensional (3-D) network structure were fabricated by pressure-less infiltration technology. The 3-D network structure reinforcement and its composites exhibited special topology structure and different fracture characteristic. Metal matrix fractured in a ductile mode is manifested by small dimples and craters on the fracture surface. When the volume fraction of reinforcement is not in excess of 6%, the composite had an improved fracture toughness. This is because of the relatively homogeneous Si_3N_4 particles distributed in the metal matrix and the occurrence of interface reaction product such as $MgAlO_2$ spinel phase. With the increases of volume fraction of reinforcement (>6%), the fracture toughness decreases slowly at the initial stages and then decreases rapidly towards the end. Therefore, the main fracture failure mechanisms consist of crack nucleation, growth, coalescence and crack propagation.

Keywords: Metal matrix composites; Fracture toughness; Fractography; Fracture mechanism

1. Introduction

Recently, magnesium alloys have shown to possess prominent application in the automotive, highway, aerospace and electronic industries where weight reduction is an important requirement. Die casting and semi-solid processing of thixotropic molding are the principal techniques for the fabrication of magnesium components. An Mg–Al–Zn (AZ91) alloy is the most widely used cast magnesium alloy, because of its superior combination of high strength at room temperature, good castability and excellent corrosion resistance. However, the poor high temperature properties of these alloys and high cost of fabricating processes have limited their use to certain specific applications [1–3]. In order to improve the high temperature properties and reduce the cost in practice, brittle properties are interpenetrated into the ductile magnesium alloy matrix. Interconnected, inter-twisted and interpenetrated composites are thus formed resulting in some novel and strong composites. The composites reinforced by 3-D network structure (3-DNSMMC) exhibited large controlled properties not only in terms of thermal conductivities but also in electrical

* Corresponding author. Address: School of Mechanical Engineering, Jinan University, Jinan 250022, China. Tel.: +86 0531 82765317.
E-mail address: Sherman0158@tom.com (S.R. Wang).

0167-8442/$ - see front matter © 2006 Elsevier Ltd. All rights reserved.
doi:10.1016/j.tafmec.2006.05.005

conductivities for the automobile, chemical and aerospace industries [4–6].

3-DNSMMC are now fabricated by a variety of techniques such as stir casting (SC) [7,8], mechanical alloying (MA) [9], powder metallurgy (PM) [10], squeeze cast (SQC) [11], molten metal infiltration (MMI) [12] and self-propagating high-temperature synthesis (SHS) [13,14]. Among all the techniques available for processing of metal matrix composites, infiltration of molten metals into reticulated porous ceramic preforms is the only technique suitable for fabricating high volume fraction (>50%) MMCs. Molten metal infiltration can be classified into three categories based on the source of driving force: pressure assisted, vacuum driven and pressure-less or capillarity driven [15]. Expensive tooling associated with pressure assisted infiltration and the limitation on the extent of pressure gradient that can be generated using vacuum, led to the exploration of new infiltration techniques such as pressure-less infiltration. Generation of positive capillary pressure when a molten metal comes into contact with a solid metal or ceramic is the governing principle of pressure-less infiltration [15]. The mechanical properties of MMCs such as elastic modulus and strength are controlled to a large extent by this fabricating technology. Especially, it is indicated the interface cohesion between the reinforcing phase and matrix is the important factor. A strong interface permits transfer and distribution of load from the matrix to the reinforcement, resulting in an increased elastic modulus and strength. On the other hand, an apparently weak bond at the reinforcement–matrix interface allows the reinforcing phase to pull out off the matrix before their full strength can be utilized. However, owing to the existence of brittle phases in inner of composites, some mechanical properties of 3-DNSMMC exhibit decreased trend. Deterioration of fracture toughness of composites reinforced by brittle phase has limited the wide applications at a certain extent. It has a great deal of significance for investigator to shed light on the fracture mechanisms of composites. There are more and more factors to affect the fracture toughness value such as the volume fracture of reinforcement, microstructure and interface characteristic, all those factors can be shown in fractography of composites. There are a lot of papers to research the fracture characteristic of metal matrix composites. Optimization of the fatigue crack arrest ability of unidirectional continuous fibre reinforced metal matrix composites is investigated by considering the damaging processes of interfacial debonding and fibre bridging [16]. A study of crack tip damage development and crack growth resistance of aluminum 359/20% silicon carbide and aluminum 6061/20% particulate reinforced metal matrix composites has been conducted [17]. A micromechanics-based elastoplastic and damage constitutive model is proposed to predict the overall mechanical behaviour of particle-reinforced metal matrix [18]. However, there are few paper to research the fracture characteristic of the metal matrix composites reinforced by the reticulated porous ceramic. In the present study, a reticulated porous ceramic (RPCs) was fabricated by twice immersing and twice sintering process, a magnesium matrix composite reinforced by three dimensional network structure was fabricated by pressure-less infiltration, the microstructure of this composite and its reinforcement were discussed and the mechanical properties of composite were tested. The target of the paper mainly concentrated on discussing the fracture characteristic in fractography of Mg–Al–Zn–Si_3N_4 composites.

2. Experimental procedure

2.1. Fabrication of RPCs

A reticulated polyurethane (PU) was chosen as a template to prepare the porous preform by replica technology. Silicon nitride (β-Si_3N_4, diameter $\leqslant$ 100 μm, Shanghai Silicon Materials Plant, China) was chosen as starting material. The microstructure of silicon nitride powder was shown in Fig. 1(a). Aluminum fine powder (which was shown in Fig. 1(b) (Al $\geqslant$ 99.26%, $D_{50} = 4 \pm 1.5$ μm, Shandong Aluminum Industry Company, China) as sintering additives were mixed with the starting material and ball-milled for 4 h using Al_2O_3 balls. Silica sol as cohesive agent was added in the powder mixture. The mixed slurry was stirred for 2 h. A commercial silica sol (SiO_2, 30.0–31.0%; pH 8.5–10.0, Shanghai Kangning Silica Sol Company, China) was used as a binder and a surfactant carboxymethyl cellulose was added to serve as a wetting agent. Kaolin (Sino Surplus International Limited, Beijing, China) and bentonite (Nanhua Hongshan Bentonite Company, Liaoning, China) were added to improve the rheology of the slurry (which content shown in Table 1).

The PUS should be cleared with deionized water before impregnation and cut into approximately $100 \times 30 \times 30$ mm samples. Then, the cleared PUS

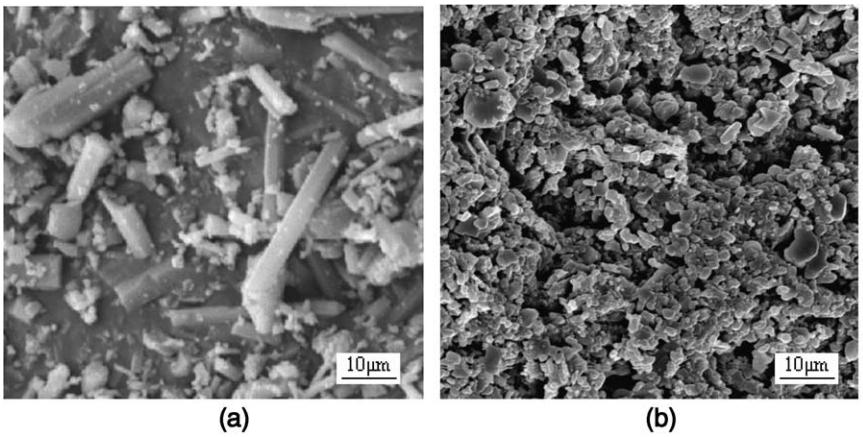

Fig. 1. SEM microstructure of Si_3N_4 starting material: (a) β-Si_3N_4 powder; (b) Al powder.

Table 1
The content of sintering additives

Aluminium (wt.%)	Alumina (wt.%)	Silica sol (wt.%)	Kaolin (wt.%)	Bentonite (wt.%)	Carboxymethyl cellulose (wt.%)	Silicon nitride (wt.%)
5	5	14.5	3.5	1	1	70

was immersed into the homogeneous slurry for about 10 min and compressed while submerged in order to fill all of the pores. The impregnated sponges passed through a preset roller to remove excess slurry. The optimum roller, Fig. 2(a), separation corresponds to about 20% of the thickness of the sponges and typically two passes are determined to remove the excess slurry. Subsequently, the samples were put into the rotating cylinder, Fig. 2(b), to obtain uniformity of struts attached by the slurry and avoid jamming the mesh of reticulated PUS by the action of centrifugal force. The rotating process is an important procedure to obtain high-open porous ceramic reinforcement. The samples were then placed in a drying oven under 160 °C for at least 20 h. Firing of the specimen was conducted in a programmable box furnace. Twice sintering and twice immersion process were used in the experiment. First, the samples were heated to 400 °C as a rate of 50 °C/h to burn out the PU framework; second, the samples were heated to 800 °C at 200 °C/h and maintained at the temperature for 60 min. Thirdly, the samples were immersed into a suspending liquid (which content shown in Table 2) for 2 h and put into the rotating cylinder and then dried for 20 h at 160 °C. To prevent the samples being jammed the mesh of ceramic foam, the suspending liquid used in the second immersion should have lower concentration than that of the slurry used in the first immersion. Subsequently, the samples were heated to

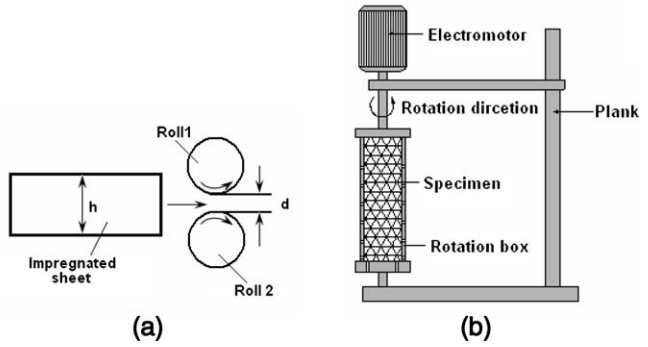

Fig. 2. Schematic diagram of squeezing and centrifugal installation: (a) installation of squeezing the excess slurry; (b) installation of centrifugal force.

Table 2
Chemical composition of Mg–Al–Zn alloy (wt.%)

Al	Zn	Cu	Mn	Fe	Si	Be	Cu	Mg
8.50	0.80	1.65	0.15	0.06	0.30	0.04	0.20	Balance

1400 °C at 200 °C/h and maintained 60 min for sintering of the ceramic powder. The novel manufacturing route for Si_3N_4 porous ceramic reinforcement is shown in Fig. 3.

DTA/TG analysis of the sponge was preformed in air atmosphere at heating rate of 10 °C/min in order to determine the thermal decomposition range. Fig. 3 showed the DTA/TG curve for the RPCs. The PUS framework was pyrolyzed and burned out gradually when the temperature was reached at 372.7 °C. An exothermic peak is observed at 632.9 °C owing to the first strong oxidation. An endothermic peak is observed at 660.2 °C which is the melting point of the aluminum metal powder. At higher temperatures of 959.1 °C, further oxidation takes place. When the temperature reaches 1261.5 °C, the glass phase occurred and acted as a medium for mass transport during densification.

Different kinds of skeletons were fabricated which have different porosity as 97%, 95%, 94%, 91%, 88%, 85%, respectively. The morphology of reticulated Si_3N_4 ceramics performs with different porosity were shown in Fig. 4 and the cross-section micrograph of reticulated Si_3N_4 ceramics performs with 94% porosity is shown in Fig. 5.

2.2. Fabrication of 3-DNSMMC

Commercial purity Al ingot (99.7% in wt.) and Mg ingot (99.95% in wt.) were used in preparing the Mg–Al–Zn alloys by melting in a clay–graphite crucible under N_2 atmosphere. The infiltrated metal used in this experiment is Mg–Al–Zn alloy which chemical compositions are shown in Table 2. The properties of Mg–Al–Zn alloy such as coefficient of thermal expansion (CTE), thermal conductivity (TC), prolongation (δ), tensile strength (σ_b) and density (D) are shown in Table 3. The porous Si_3N_4 ceramic skeleton was heated up in a furnace under nitrogen atmosphere. After achieving the appointed temperature, the liquid metal was infiltrated into the perform in the infiltration die by pressure-less infiltration technology (which schematic representation of infiltration die is shown in Fig. 6). The micro-structural characterization of ceramic–metal composites was performed on a scanning electron microscope (SEM, Hitachi, S-2500) which was shown in Fig. 7. In Fig. 7, the relative density of reinforcement (volume fraction of reinforcement) is 6%, 9%, 12%, 15%, respectively. The morphology of Mg–Al–Zn–Si_3N_4 composites with the relative density of reinforcement (volume fraction of reinforcement) as 6% is shown in Fig. 8. The interface element concentration grads distributing were carried out by the energy spectrum analyses (ESA, OXFOED INCA).

2.3. Bending strength and fracture toughness

The specimens were determined at the condition of cast and no heat-treatment. The mechanical

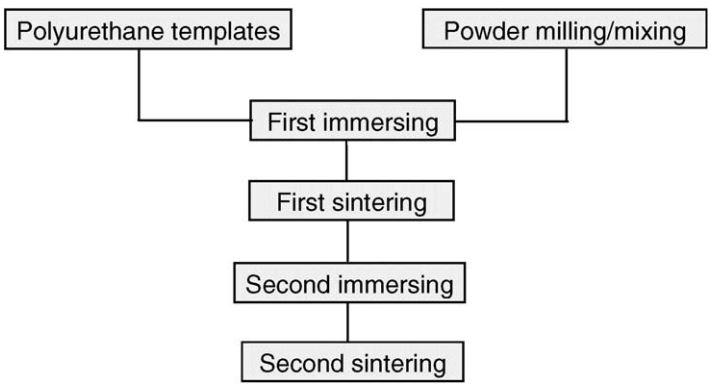

Fig. 3. Novel manufacturing route for Si_3N_4 RPCs.

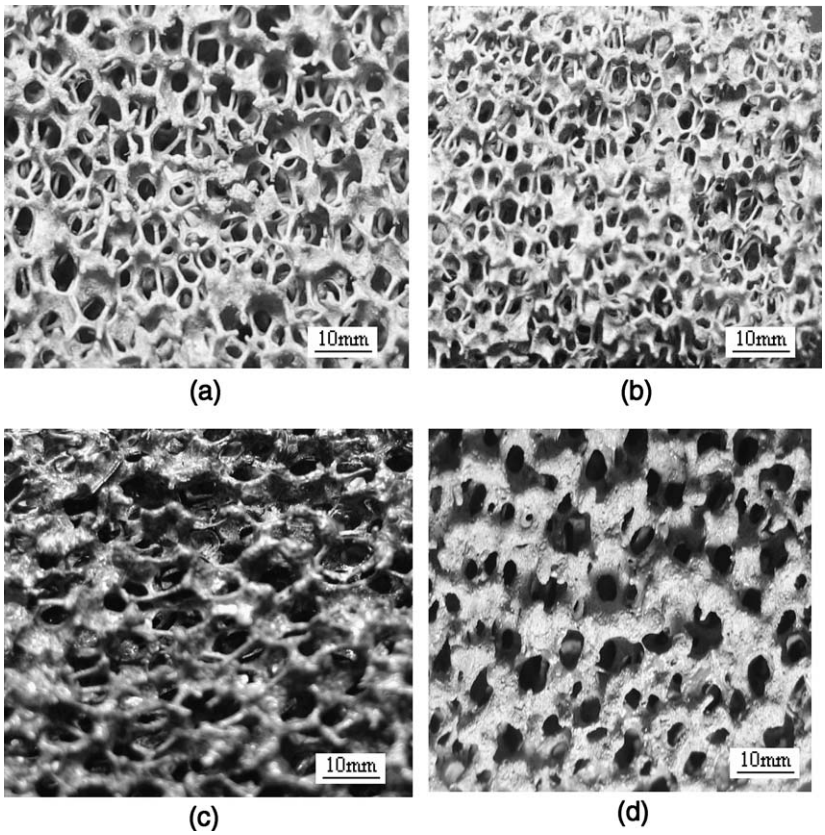

Fig. 4. The morphology of reticulated Si_3N_4 ceramics perform with different porosity: (a) 94%; (b) 91%; (c) 88%; (d) 85%.

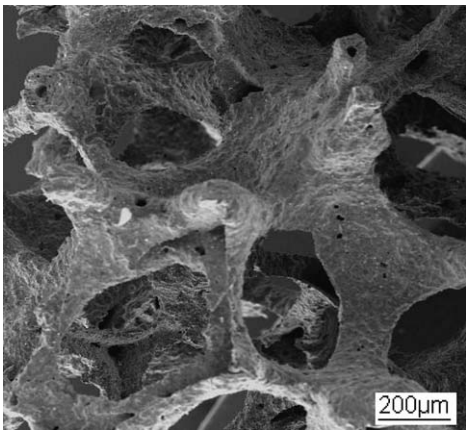

Fig. 5. The morphology of reticulated Si_3N_4 ceramics performs with 94% porosity.

Table 3
Mechanical properties of Mg–Al–Zn alloy

Materials	CTE (10^{-6} C^1)	TC (w m C^{-1})	δ (%)	σ_b (MPa)	D (g cm^{-3})
Mg–Al–Zn	28.1	78.5	3.3	230	1.8

properties tests as three point (3-P) bending strength were carried out on the electron omnipotence testing machine (Instron5569). The specimens were loaded at a constant cross-head speed of 10^{-2} cm s^{-1}. The geometry structure was shown in Fig. 9. The dimensions of specimen were shown in Table 4. Fractographs of all the broken specimens tested under 3-P bending conditions were observed using a scanning electron microscope (SEM, Hitachi, S-2500). The notch was cut through electro-discharge machining which has a geometry characteristic of root radius of 200 μm, normal width of 2 mm and a normal length of approximately 3–4 mm.

3. Test results and discussion

3.1. Microstructure of RPCs

Si_3N_4 offered the potential for development as a high strength, high temperature refractory material, so it is the appropriate and preferred materials as

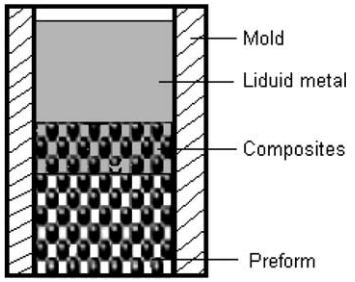

Fig. 6. Schematic representation of infiltration die.

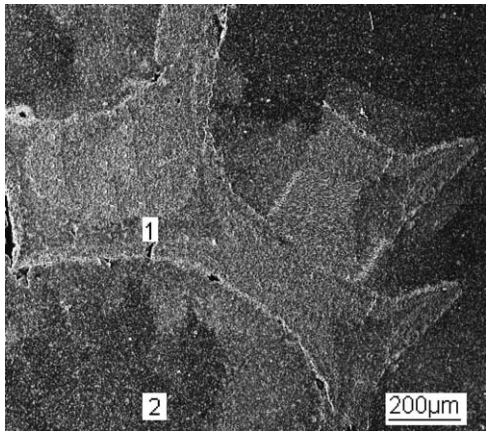

Fig. 8. The morphology of Mg–Al–Zn–Si_3N_4 composites with 6% reinforcement.

the reinforcement of metal matrix composites. However, it was soon recognized that pure Si_3N_4 could not be fabricated into fully dense components because of its strong covalent bonding. Alternative methods have therefore been explored and one of the most successful fabrication techniques is liquid phase sintering using a metal silicon oxynitride based liquid. For this purpose it is necessary to add small amounts of metal oxides, which at sintering temperature react with the natural surface SiO_2 on the Si_3N_4 powder, particles and with the Si_3N_4 itself, to form a liquid. The liquid phase assists particle rearrangement and acts as a high diffusivity pathway for the subsequent solution–diffusion–precipitation process. Generally, the constituents of

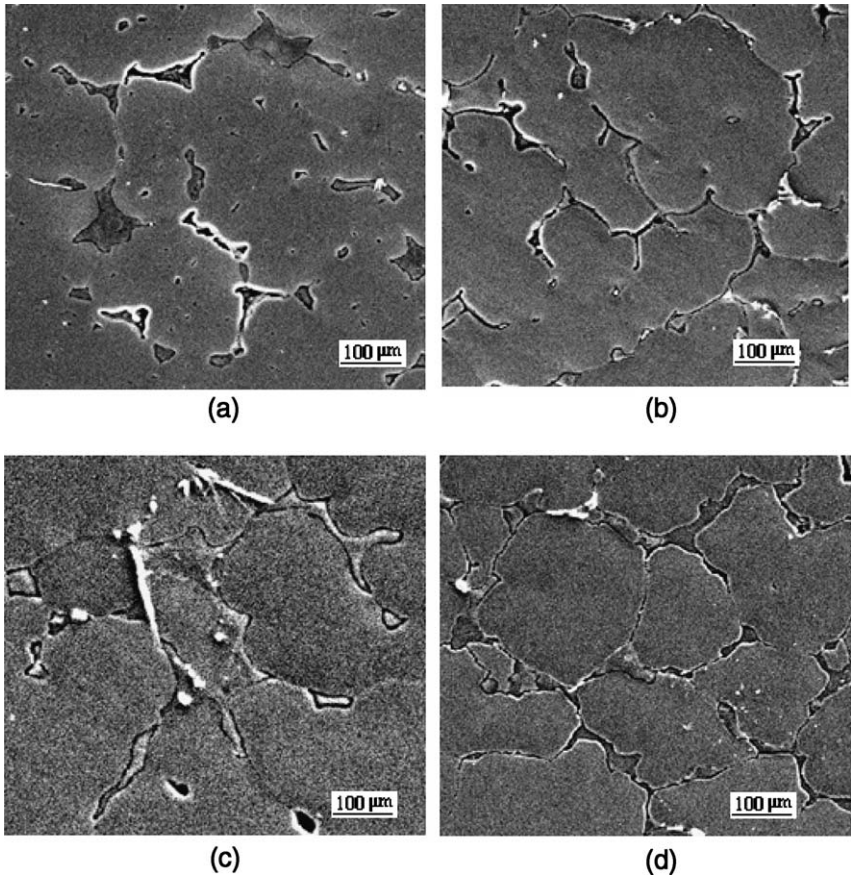

Fig. 7. The SEM micrographs of 3DCNRMMC with different volume fracture reinforcement: (a) 6%; (b) 9%; (c) 12%; (d) 15%.

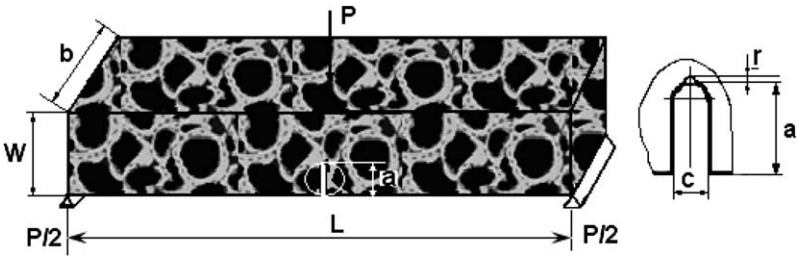

Fig. 9. Specimen of bending strength.

Table 4
Dimensions of specimen

Materials	L (mm)	w (mm)	b (mm)	a (mm)	c (mm)	r (μm)	a/w
Mg–Al–Zn/Si_3N_4	85	20	15	3.0–4.0	2	200	0.20–0.27

this liquid phase cannot be completely incorporated into the Si_3N_4 lattice, and they remain either as a glass, or as a crystalline metal silicon oxynitride phase in the intergranular region of the Si_3N_4 ceramic [19]. The intrinsic properties of a material, especially at high temperature, are determined by the content and type of sintering additive; different sintering aids yield different phase compositions and microstructures. Al as low temperature sintering additives was melted and oxidized into Al_2O_3 in the course of sintering and jammed the hollow struts. Al_2O_3 as high temperature sintering additives would improve the density of struts. In situ SiO_2 phase would be formed in high temperature and oxidation atmosphere. One multiphase ceramic foam as Si_3N_4–Al_2O_3 (oxidation + addition)–SiO_2 (oxidation + in situ) was formed. The cross-section micrographs of RPCs are shown in Fig. 10.

The relative density (ρ^*/ρ_s – relative density, ρ^* – the density of porous structure and ρ_s – the density of the fully dense material) as a important property of cellular ceramic was measured using the Archimedes' method. The porosity of RPCs was related with the relative density. The pore size and the width of strut(t) and the length of strut(l) were measured from Fig. 5, in which, the cross-section and surface micro-structural characterization of the samples were performed on a scanning electron microscopy SEM (Model No. S-2500). The number of pore could be counted and the obtained results are presented in Table 5. The parameters of ceramic foam as hexagonal side of pore, cell volume and struts surface area were obtained from Appendix A. The relative density was validated by the formula described in Appendix A and the calculation result are presented in Table 6.

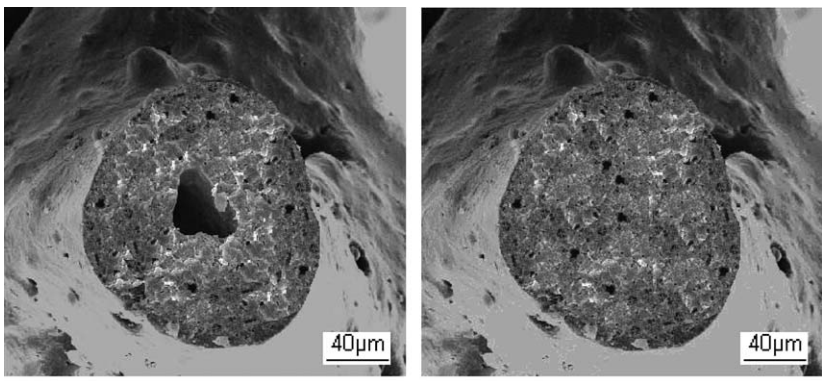

Fig. 10. SEM cross-section micrographs of RPCs: (a) no additives; (b) additives of 5% Al and 5% Al_2O_3.

Table 5
Parameters of porous ceramic skeleton

Sample	The number of pore (ppi)	Pore size (d, mm)	Struts width (t, mm)	Struts length (l, mm)
B	5–10	1–3	1.2–2.7	4–7

Table 6
Density and porosity of porous ceramic skeleton

Sample	Skeleton density (g/cm^3)	Density of material (g/cm^3)	Relative density (g/cm^3)	Calculation result (g/cm^3)	Open porosity (%)
A	0.51	3.17	0.16	0.166	84
B	0.47	3.17	0.15	0.154	85
C	0.46	3.17	0.14	0.150	86

3.2. Microstructure of 3-DNSMMC

3-DNSMMC exhibit a specially topology structure with each brittle and ductile phase interconnected in three dimensions and constructed a topologically continuous network throughout the microstructure. Fig. 8 shows microstructure morphology of 3-DNSMMC. It can be seen that Mg–Al–Zn alloy was fully intruded into the channel of RPCs. The fabricated composites have topologically uniform microstructure and the interconnected network structure is evident. In this figure, the regions marked 1 represent RPCs, which are interpenetrated by Mg–Al–Zn alloy (regions marked 2). The interface of metal/ceramic plays an important role in improving the mechanical properties. In the interface of Mg–Al–Zn–Si_3N_4 composites, $MgAl_2O_4$ spinel forms at the ceramic/metal interface. It can take place during the process of pressureless infiltration of melted magnesium into the porous Si_3N_4 ceramic network structure. During the fabrication processes, the strut surface of Si_3N_4 ceramic formed a oxide film of Al_2O_3 and SiO_2 due to the ceramic materials sintered at oxidizing atmosphere, Mg reacts with Al_2O_3 and reacts with Al and SiO_2, the reactants form glass phase which some surround the Si_3N_4 grain and some distribute on the surface of struts of RPCs. In the same time, the spinel phases form a thin layer between the metal and ceramic side. Thus interface structure became the transition zone to release the strain and amortize the over loading.

3.3. Bending strength and fracture toughness

Owing to the phenomenon of ductile melt metal interpenetrating into brittle reinforcement, the bending strength and fracture toughness exhibit different properties to metal matrix and reinforcement. The three point bending strength (σ_f) was calculated using the equation as follows:

$$\sigma_f = \frac{3PL}{2bw^2} \tag{1}$$

where P is the load, w is the specimen thickness, b is the specimen width and L is the specimen length. The fracture toughness (K_{IC}) value was calculated using the equation as follows:

$$K_{IC} = Y\left(\frac{a}{w}\right)\frac{3PL}{2bw^2}\sqrt{a} \tag{2}$$

where a the notch height, $Y(a/w)$ is a complex function of a/w, a non-dimensional coefficient which value relates to a/w and constant cross-head speed. $Y(a/w)$ value may be chosen according to Fig. 11 [20]. The experimental data were applied in Eq. (2) and the calculation results were taken an average of two measurements which were shown in Figs. 12 and 13.

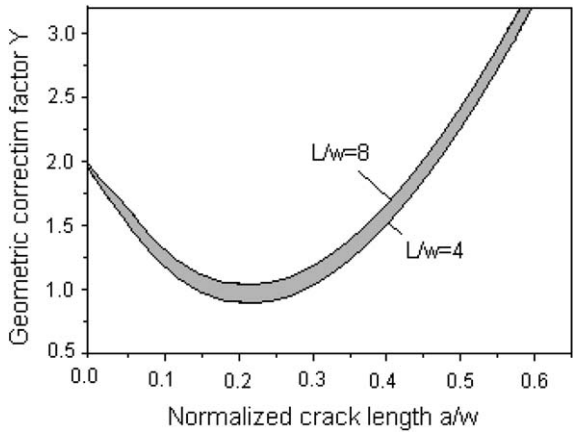

Fig. 11. Relationship between Y and a/w for specimen of bending strength.

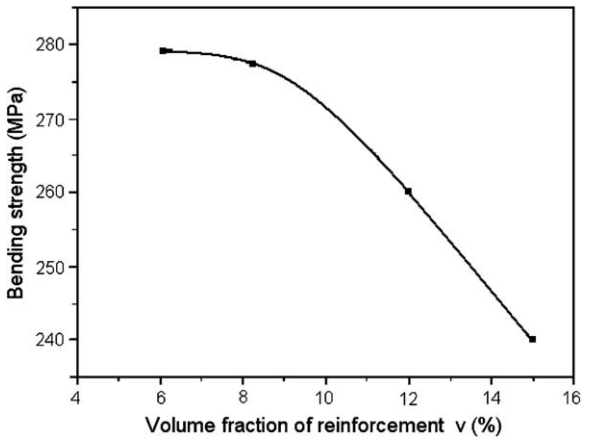

Fig. 12. Relation between bending strength and volume fraction of reinforcement.

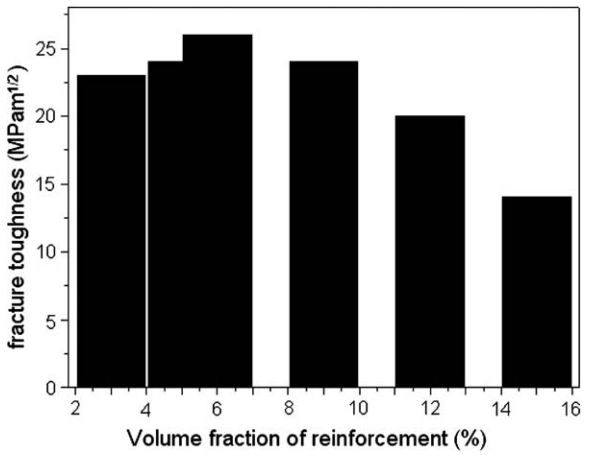

Fig. 13. Relation between fracture toughness and volume fraction of reinforcement.

Fig. 12 shows the relationship between bending strength and volume fraction of reinforcement. Fig. 13 shows the relationship between fracture toughness and volume fraction of reinforcement. From Fig. 12, it can be seen that, there is a little elevation of the bending strength value of reinforced composites compared with the un-reinforced materials. 3-DNSMMC with volume fraction of reinforcement as 6% exhibit a bending strength of 276 MPa. Subsequently, with the increases of volume fraction of reinforcement (>6%), the bending strength decreases slowly at initial stages and then decreases rapidly in the end.

From Fig. 13, the K_{IC} curve accord approximately to linear rule with a gradual descendent decreases trend. 3-DNSMMC with volume fraction of reinforcement as 6% exhibit a fracture toughness K_{IC} of 25.5 MPa $m^{1/2}$. It is indicated that the volume fraction of reinforcement plays a significant role in controlling the bending strength and fracture toughness. It is simultaneously indicated that the bending strength is lower than metal matrix for 3-DNSMMC if the volume fraction is in excess of 6%. Owing to the exist of brittle phases, the failure features as cracking and void in reinforcement, interface cracking and interface debonding as well as matrix damage result in the decreases of bending strength and fracture toughness. Owing to the brittle phase interpenetrating in ductile phase and dissevering metal matrix, there is no possibility for fracture toughness of reinforced composites (>6%) to be in excess of that of matrix metal. The reason why K_{IC} has an obvious increase when the volume fraction of reinforcement cannot exceed the percentage of 6% is that molten metal infiltrated not only into the pore of 3-D network skeleton but also into the interior of struts of skeleton. This may be validated by the energy spectrum analyses (ESA, OXFOED INCA) which were shown in Fig. 14. The contents of Mg, Al and Zn in Si3N4 reinforcement are still high. It is indicated that the void and crack in ceramic skeleton are clogged up by molten metal and its reactant.

3.4. Fractography

Fig. 15 shows the fractographs of Mg–Al–Zn alloy and composites reinforced with different percentage of reinforcement. Owing to the adequate ductility of Mg–Al–Zn alloy, much and smaller dimples and crater are observed in SEM fractographs, Fig. 15(a). The crater coalescence is the predominant failure mode of metal matrix. This phenomenon has been early observed by many investigators [21–23,3]. When the second brittle phases were introduced to the metal matrix, the SEM fractographs present two different failure mechanisms as a locally ductile failure mechanism and crack expanding failure mechanism. With the increases of volume fraction of reinforcement, there is a distinguished difference in composites, Figs. 15(b)–(e), the limited ductility of composites causes the early failure of composites.

From Fig. 15(b), it can be shown that, big craters and dimples with a bimodal and multimodal distribution characteristic were observed. A large number of ceramic particle were engulfed in crater enclosed by surrounded matrix which marked arrow. The

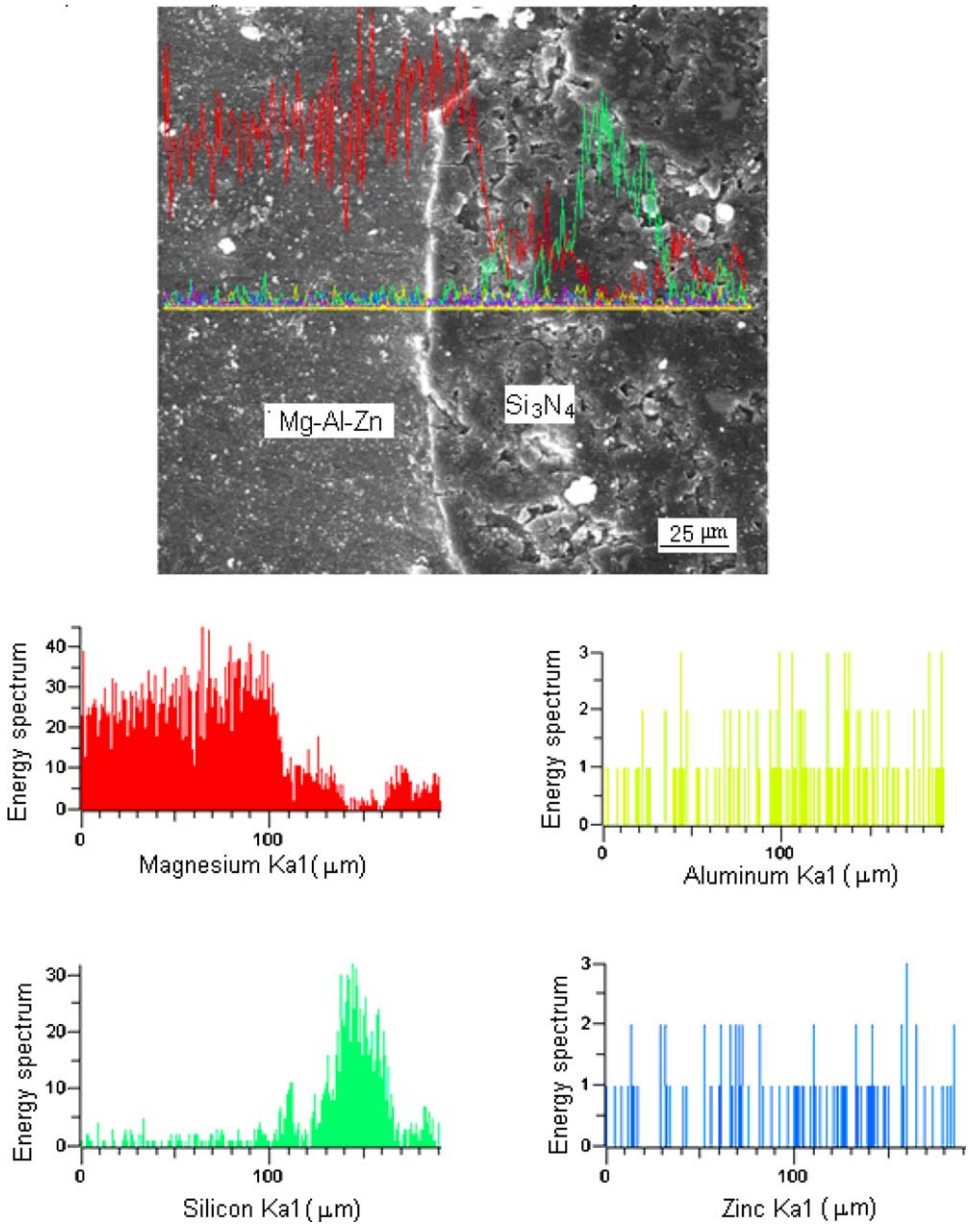

Fig. 14. The interface of Mg–Al–Zn–6%Si_3N_4 composites and the energy spectrum analyses (ESA, OXFOED INCA).

relatively homogeneous Si_3N_4 particle distribution which were immersed and encircled by metal matrix results in the improvement of fracture toughness. Moreover, lightly interface reaction occurred in the metal–ceramic interface produced $MgAlO_2$ spinel phase (Fig. 16) which became the transition between the brittle phase and ductile phase. Therefore, the reactant baffles the crack propagation in ceramic/metal interface and improved the bonding strength of ceramic–metal composites.

Ceramic struts of skeleton turn more and more distinct in Fig. 15(c) (arrow 1). A large number of cracks were embodied into the skeleton to make the composites fracture easily at low stress. Interface debonding of matrix/Si_3N_4, arrow 2, Fig. 15(c), is another reason for failure. With the increases of volume fraction of reinforcement, crack characteristic consist of crack nucleation, growth, coalescence and crack propagation became the main fracture failure mechanisms.

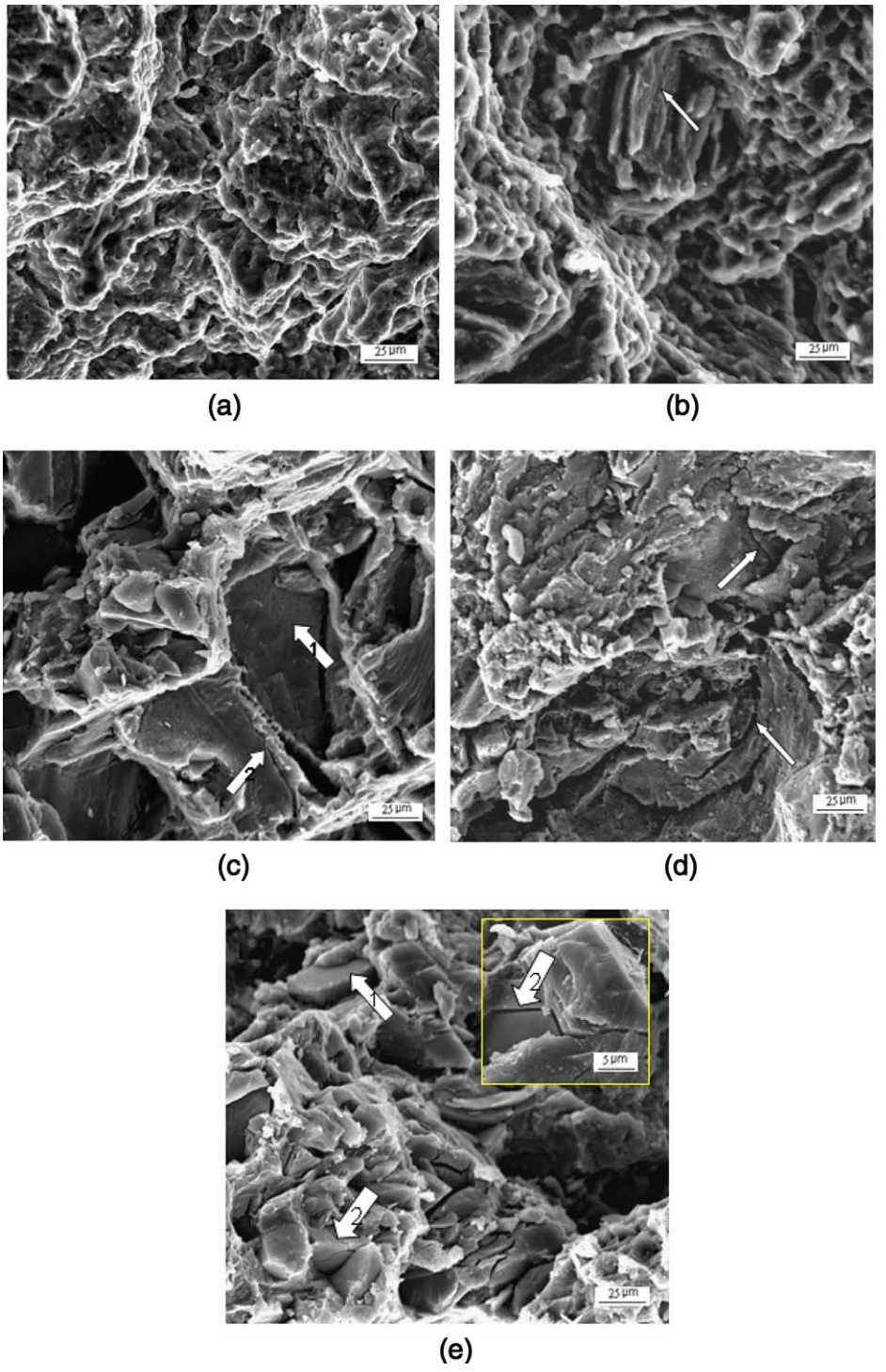

Fig. 15. Fractographs of Mg–Al–Zn alloy and reinforced composites with different percentage of reinforcement: (a) Mg–Al–Zn alloy; (b) 6%Si_3N_4; (c) 9%Si_3N_4; (d) 12%Si_3N_4; (e) 15%Si_3N_4.

From Fig. 15(d), owing to the matrix deformation, stress transfer to ceramic reinforcement causing occurrence of crack fountainhead (microcracks). Microcracks grow continuously and are coalesced endlessly. Finally microcracks were propagated and enlarged into large crack, arrow in Fig. 15(d).

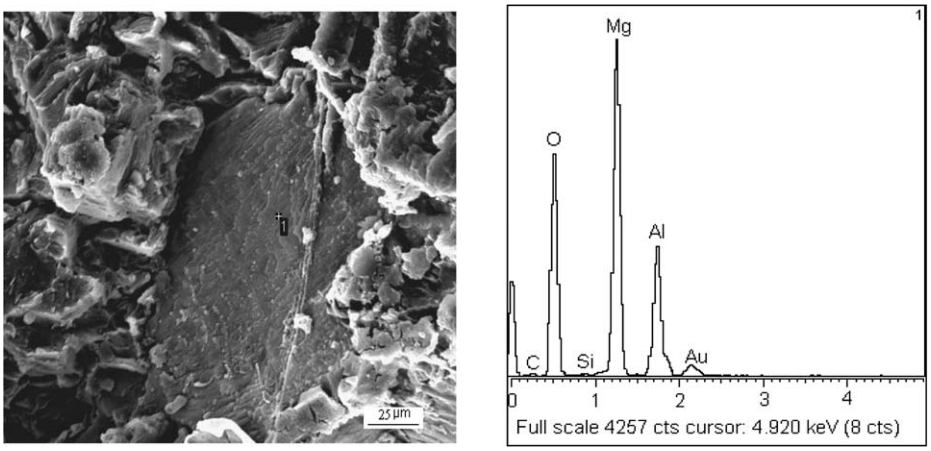

Fig. 16. Spinel phase in SEM fractographs of Mg–Al–Zn–6%Si_3N_4 composites.

Fig. 15(e) depicts the SEM fractographs characteristic of Mg–Al–Zn–15%Si_3N_4 composites. From Fig. 15(e), a great deal of ceramic particles with regular shape, arrow in Fig. 15(e) is observed distinctly. Much cracks occurred in the regions of the particle interior and particle border. When examined at higher magnifications, the fractured Si_3N_4 particles show a clear crack running through the center of the particle, Fig. 15(e), arrow 2. These factors result in the fracture of these kinds of reinforcements under low stresses.

4. Conclusions

1. One kind of 3-D ceramic–metal MMCs with different volume fraction reinforcement was fabricated by pressure-less technique. The bending strength and fracture toughness were tested by 3-P bending strength experiments.
2. Mg–Al–Zn–6%Si_3N_4 composites had an improvement of bending strength and fracture toughness owing to relatively homogeneous Si_3N_4 particle distribution encircled by metal matrix, the occurrence of interface reaction product as $MgAlO_2$ spinel phase.
3. With the increases of volume fraction of reinforcement (>6%), the bending strength and fracture toughness decreases slowly at initial stages and then decreases rapidly in the end. Owing to the exist of brittle phases, the failure features as cracking and void in reinforcement, interface cracking and interface debonding as well as matrix damage result in the decreases of bending strength and fracture toughness.
4. 3-DNSMMC have different SEM fractographs characteristic with matrix metal and different volume fraction of reinforcements. Much and smaller craters and dimples are observed in metal matrix alloy and limited ductility of composites causes the early failure of composites. With the increases of volume fraction of reinforcement, crack characteristic consist of crack nucleation, growth, coalescence and crack propagation became the main fracture failure mechanisms.

Acknowledgement

This research was granted by Natural Science Foundation of China (50371047).

Appendix A

Properties	Symbol	Formula
Pore diameter	d_p	Measured
Relative density	$\frac{\rho^*}{\rho_s}$	$C_1\left(\frac{t}{l}\right)^2\left(1-C_2\left(\frac{t}{l}\right)\right)$
Solid proposity	p	Measured
Hexagonal side	l	$\frac{0.5948 d_p}{1-0.97(1-p)^{\frac{1}{2}}}$
Struts thickness	t	$0.971(1-p)^{\frac{1}{2}} l$

References

[1] P.K. Biswas, S.C. Dev, C.S.S. Krishnan, Mg alloys and composites as the future challenging materials for automobile applications, Ind. Foundry J. 45 (3) (1999) 17–26.

[2] A. Luo, M.O. Perquleryuz, Review – cast Mg alloys for elevated temperature applications, J. Mater. Sci. 29 (1994) 5259–5271.

[3] S. Jayalakshmi, S.V. Kailas, S. Seshan, Tensile behaviour of squeeze cast AM100 magnesium alloy and its Al_2O_3 fibre reinforced composites, Composites: Part A 33 (2002) 1135–1140.

[4] M. Hoffman, S. Skirl, W. Pompe, J. Roedel, Thermal residual strains and stresses in Al_2O_3/Al composites with interpenetrating networks, Acta Mater. 47 (1999) 565–577.

[5] L.D. Wegner, L.J. Gibson, The mechanical behaviour of interpenetrating phase composites I: modeling, Int. J. Mech. Sci. 2 (2004) 925–942.

[6] Helge Prielipp, Mathias Knechtel, Nils Claussen, S.K. Streffer, H. Mullejans, M. Ruhle, Jurgen Rodel, Strength and fracture toughness of aluminum/alumina composites with interpenetrating networks, Mater. Sci. Eng. A 197 (1995) 19–30.

[7] Q.C. Jiang, H.Y. Wang, J.G. Wang, Fabrication of TiCp/Mg composites by the thermal explosion synthesis reaction in molten magnesium, Mater. Lett. 57 (2003) 2580–2583.

[8] R.A. Saravanan, M.K. Surappa, Fabrication and characterization of pure magnesium 30 vol% SiCp composites, Mater. Sci. Eng. A 276 (2000) 108–116.

[9] L. Lu, K.K. Thong, M. Gupta, Mg-based composite reinforced by Mg_2Si, Compos. Sci. Technol. 63 (2003) 627–632.

[10] H. Ferkel, B.L. Mordike, A structure materials properties microstructure and processing, Mater. Sci. Eng. A 298 (2001) 193–199.

[11] A.L. Filho, H. Atkinson, H. Jones, Hot isostatic pressing of metal reinforced metal matrix composites, J. Mater. Sci. 33 (1998) 5517–5533.

[12] S.K. Thakur, B.K. Dhindaw, The influence of interfacial characteristics between SiCp and Mg/Al metal matrix on wear, coefficient of friction and microhardness, Wear 247 (2001) 191–201.

[13] Q.C. Jiang, H.Y. Wang, Q.F. Guan, Effect of the temperature of molten magnesium on the thermal explosion synthesis reaction of Al–Ti–C system for fabricating TiC/Mg composite, Adv. Eng. Mater. 10 (2003) 722–725.

[14] H.Y. Wang, Q.C. Jiang, X.L. Li, Fabrication of TiC particulate reinforced magnesium matrix composites, Scr. Mater. 48 (2003) 1349–1354.

[15] B. Srinivasa Rao, V. Jayaram, Pressureless infiltration of Al–Mg based alloys into Al_2O_3 preforms: mechanisms and phenomenology, Acta Mater. 49 (2001) 2373–2385.

[16] C.A. Rodopoulos, E.R. de los Rios, J.R. Yates, Optimising the crack arrest ability of unidirectional metal matrix composites, Int. J. Fatigue 21 (1999) 1007–1012.

[17] J.W. Leggoe, X.Z. Hu, M.B. Bush, Crack tip damage development and crack growth resistance in particulate reinforced metal matrix composites, Eng. Fract. Mech. 53 (6) (1996) 873–895.

[18] L.Z. Sun, H.T. Liu, J.W. Ju, Effect of particle cracking on elastoplastic behaviour of metal matrix composites, Int. J. Numer. Methods Eng. 56 (2003) 2183–2198.

[19] Tatli Zafer, P. Thompson Derek, Densification behaviour of oxide-coated silicon nitride powders, Mater. Lett. 59 (2005) 1897–1901.

[20] W.F. Brown, Jr., J.E. Srawley, Plane strain crack toughness testing of high strength metallic materials, ASTES.T.P. 410, ASTM, Philadelphia, 1966.

[21] P. Cavaliere, Mechanical properties of friction stir processed 2618/Al2O3/20p metal matrix composite, Composites: Part A 36 (2005) 1657–1665.

[22] Y. Png, T.K. Chaki, Fatigue damage in a unidirectional SiC/Al composites due to push-pull and zero-pull loading, Mater. Sci. Eng. A 200 (1995) 38–48.

[23] S.C. Sharma, B.M. Girish, D.R. Somashekar, Rathnakar Kamath, B.M. Satish, Mechanical properties and fractography of zircon-particle-reinforced ZA-27 alloy composite materials, Compos. Sci. Technol. 59 (1999) 1805–1812.